LJMU Research Online

Yang, Y, Bashir, M, Wang, J, Michailides, C, Loughney, S, Armin, M, Hernandez, S, Urbano, J and Li, C

 Wind-Wave Coupling Effects on the Fatigue Damage of Tendons for a 10 MW Multi-Body Floating Wind Turbine

http://researchonline.ljmu.ac.uk/id/eprint/13517/

Article

For more information please contact researchonline@ljmu.ac.uk

Wind-Wave Coupling Effects on the Fatigue Damage of Tendons for a 10 MW Multi-Body Floating Wind Turbine

Yang Yang [a,d], Musa Bashir [a,*], Jin Wang [a], Constantine Michailides [b], Sean Loughney [a], Milad Armin [a], Sergio Hernández [c], Joaquín Urbano [c], Chun Li [d]

[a.] Liverpool Logistics, Offshore and Marine (LOOM) Research Institute, Liverpool John Moores University, Liverpool, Byrom Street, L3 3AF, UK,

[b.] Department of Civil Engineering and Geometrics, Cyprus University of Technology, Limassol, Saripolou 2-8, 3036, Cyprus

[c.] Offshore Division. ESTEYCO SA. Menéndez Pidal 17, 28036 Madrid, Spain.

[d.] School of Energy and Power Engineering, University of Shanghai for Science and Technology, Shanghai, 200093, P.R. China;

Abstract: This study investigates the wind-wave coupling effects on fatigue damage of tendons that connect multiple bodies of a novel floating platform (TELWIND) supporting a 10 MW wind turbine. An aero-hydro-servo tool is developed for dynamic analysis of a multi-body floating wind turbine (FWT) platform, by incorporating AeroDyn with AQWA through a user-defined dynamic library link (DLL) to conduct simulations of the FWT subjected to wind, wave and current loadings. The comparison against FAST has validated the accuracy of the AQWA-AeroDyn coupling framework in predicting coupled responses of the FWT. A specific site in the northern coast of Scotland is selected and design load cases are examined for the estimation of the fatigue damage of the tendons of the FWT. In the absence of wind-wave coupling, the motion differences between the two bodies of the platform are larger, leading to 43.7% enhancement in the tension fluctuation of tendons in average. Consequently, the fatigue damage of the tendons is significantly overestimated. Also, the investigation on the influence

* Corresponding author: m.b.bashir@ljmu.ac.uk

of effective simulation length on the fatigue damage shows that 90% accuracy can be achieved when 20% of the simulation analysis length is decreased.

Key words: Multi-body platform; Floating Wind Turbines; ARCWIND; Aero-Hydro-Servo Coupled Method; Fatigue Analysis; Tendons

1. Introduction

The technology of offshore wind energy extraction is continuing to receive more attention due to its maturity, abundance of offshore wind reserves and the role of wind energy as an alternative to fossil fuels. It is expected that no less than 55 GW of wind turbines would be installed each year until 2023 [1]. One of the main goals of recent studies on offshore wind energy utilization has been to reduce the levelized cost of electricity (LCOE). With the increase of wind turbine scale, the up-front costs are decreased through economies of scale and reduced plant costs on a per megawatt basis. The performance of large scale wind turbines with taller towers and longer blades is better than that of small wind turbines. In addition, large scale offshore wind turbines offer the advantage of reduced frequency of transportation, installation and maintenance related activities. In combination, these trends have reduced the LCOE of an offshore wind farm made of large wind turbines [2]. Compared to a fixed-bottom type, the floating type is more suitable for large-scale (10+ MW) offshore wind generation applications because it can operate in deeper seas where more abundant wind resources exist.

The past decade has witnessed the developments of numerous floating platform concepts for wind turbines. In 2009, Statoil developed a spar-buoy in the Hywind project for the world first full-scale FWT. This was followed by the modification of the Hywind spar-buoy by National Renewable Energy Laboratory (NREL) to support the NREL 5 MW wind turbine in the Offshore Code Comparison Collaboration (OC3) project sponsored by the International

Energy Agency (IEA) in 2010 [3]. The OC3-spar platform has been extensively used in various studies for further development of offshore wind energy system [4-6]. In addition, NREL developed a semi-submersible platform in the subsequent DeepCwind project [7] and a tension leg platform (TLP) based on the Massachusetts Institute of Technology design concept [8] as part of the OC4 and OC5 projects, respectively. Three 1/50th scaled models of the NREL's spar, semi-submersible and TLP were tested in different environmental conditions to provide sufficient experimental data for validating the numerical analysis tools of floating wind turbines (FWTs) [9]. Dynamic responses of the NREL's spar, TLP and a barge [10] supporting the NREL 5 MW wind turbine were compared quantitatively.

However, the capacity of wind turbines supported by aforementioned floating platforms were limited to 5 MW. It is noted that the offshore applications of higher capacity wind turbines (≥ 10 MW) have been the focus of research in the recent years due to their high potentials in reducing LCOE [11-12] of FWTs in deep sea areas. European Union (EU) has been at the forefront in funding some pioneering projects in developing floating platforms for 10 MW-class wind turbines. For instance, the INNWIND project [13] proposed a semi-submersible concept for the DTU (Technical University of Denmark) 10 MW wind turbine. Hydrodynamic performance of the platform was investigated. The LIFE50+ project [14] has developed four floating concepts for 10 MW wind turbines, including two semi-submersible platforms made of concrete and steel, a concrete barge platform and a steel TLP. HAWC2 and FAST were used as the numerical analysis tools to conduct the coupled analysis after comparisons against wave tank experiments comprehensively. More recently, a free-float capable TLP [15] was developed in the ARCWIND project for 10 MW wind turbines. The hydrodynamic performance of the platform under operational and 50-year extreme conditions was evaluated and the results verified the survivability of the structure. In addition, the ARCWIND project employed a novel two-body spar floating platform (called "TELWIND platform") developed

by ESTEYCO [16] for 10+ MW FWTs applications. The TELWIND platform consists of two concrete tanks: an upper tank (UT) which provides buoyancy and a ballasting lower tank (LT) providing pitch stability. The UT and the LT are connected by 6 tendons which are designed to always be in tension to ensure a low centre of gravity (CoG) of the platform, as shown in Fig. 1. It is apparent that the safety and stability of the FWT significantly depend on the integrity of the tendons. Therefore, it is imperative to conduct fatigue assessment of the tendons for this particular platform.
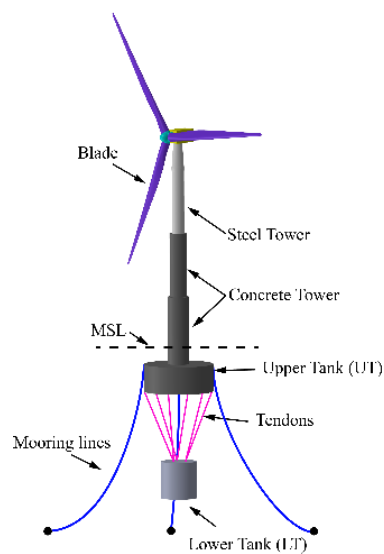

Fig. 1: TELWIND platform concept

As revealed in the recent studies [17-22], dynamic responses of a FWT are affected by the interactions between aerodynamic loads and hydrodynamic loads. Therefore, the wind-wave coupling effect must be taken into account when evaluating fatigue life of the multi-body platform tendons. It is noted that the commonly used numerical tools have limitations in their capability to examine the dynamic responses of a multi-body floating platform connected by flexible elements.

In order to address these limitations, this study has developed a coupled numerical method for multi-body floating platforms by incorporating AeroDyn with AQWA through a user-defined DLL. The developed generic numerical method is applied for fatigue analysis of the

tendons of the multi-body platform after validating against FAST. The design load cases for the fatigue assessment are defined according to the observed met-ocean data during the period from 2011 to 2016 in a specified site off the northern coast of Scotland. A comparative analysis of fatigue damage of the tendons between the coupled method and decoupled method analysis is performed in order to quantitatively evaluate the wind-wave coupling effects. For the coupled method, the responses of the wind turbine due to wind, wave and current excitations are coupled through the user-defined DLL, while for the decoupled method the aerodynamic loads of the wind turbine are calculated independently of the platform motions and are then used together with hydrodynamic loads for solving the equation of motion in time domain. Based on the time domain results obtained from both the coupled and decoupled analysis, fatigue damage of each of the tendons is predicted in accordance with the International Electrotechnical Commission (IEC) standard [23]. The wind-wave coupling effects on the fatigue damage of the tendons of the TELWIND multi-body platform are determined and discussed. In addition, the influence of the simulation duration is examined and quantified using the coupled method.

2. Wind turbine model

2.1 DTU 10 MW baseline wind turbine

DTU developed a reference 10 MW wind turbine in collaboration with Vestas in the Light Rotor project [11]. The three-bladed wind turbine has been classed as an IEC class 1A wind climate with a rated wind speed of 11.4 m/s. A simple nacelle and a drivetrain were also designed for the DTU baseline wind turbine. Due to availability of the detailed aerodynamic shape and structural properties in public domain, the DTU 10 MW wind turbine has been widely used for the development of various offshore support structures. Table 1 presents a summary of design parameters of the DTU reference wind turbine. It is noted that the FWT

supported by the multi-body platform has the same hub height as the DTU 10 MW reference wind turbine.

Table 1: Specifications of the DTU 10 MW reference wind turbine

Property (Unit)	Value
Rated power (MW)	10.0
Rated wind speed (m/s)	11.4
Cut-in/cut-out wind speed (m/s)	4.0/25.0
Minimum/rated rotor speed (rpm)	6.0/9.6
Rotor diameter (m)	178.3
Hub diameter (m)	5.6
Gearbox ratio (-)	50
Shaft tilt angle (degrees)	5.0
Pre-cone angle (degrees)	-2.5
Rotor mass (kg)	227,962
Nacelle mass (kg)	446,036
Hub height (m)	119.0

2.2 Description of the 10 MW multi-body model

The TELWIND model is originally developed by ESTEYCO for the floating application of offshore wind turbines. The floating platform consists of two bodies (UT and LT) connected by six tendons. The UT is designed to provide buoyancy while the LT is for ballasting to ensure stability of the whole wind turbine system. The two bodies are made of concrete in order to reduce the cost. A telescopic tower is incorporated in the platform to ease the transport and installation processes. The tower consists of three sections: a topmost steel section that directly supports the turbine and two lower sections made of concrete. It is noted that the tower has a much higher bending stiffness compared to the DTU reference tower. More specifically, the tower-base bending stiffness of the TELWIND concept is 1.30×10^{13} N·m^2, while the bending stiffness of the 10 MW DTU reference tower at the base is 1.77×10^{12} N·m^2.

Fig. 2 presents a schematic diagram of the 10 MW multi-body wind turbine which is applicable to 110 m water depth areas or deeper seas with appropriate modifications on mooring lines configuration. The UT is 10 m below the mean sea level (MSL) with a draught

of 16.75 m. The LT has a draught of 22.5 m and the total draught of the combined structure is 92.25 m. The diameters of UT and LT are 44.5 m and 23.0 m, respectively. Each of the tendons has a length of 48.81 m and an equivalent diameter of 0.271 m. In AQWA, each tendon is modelled as a catenary.
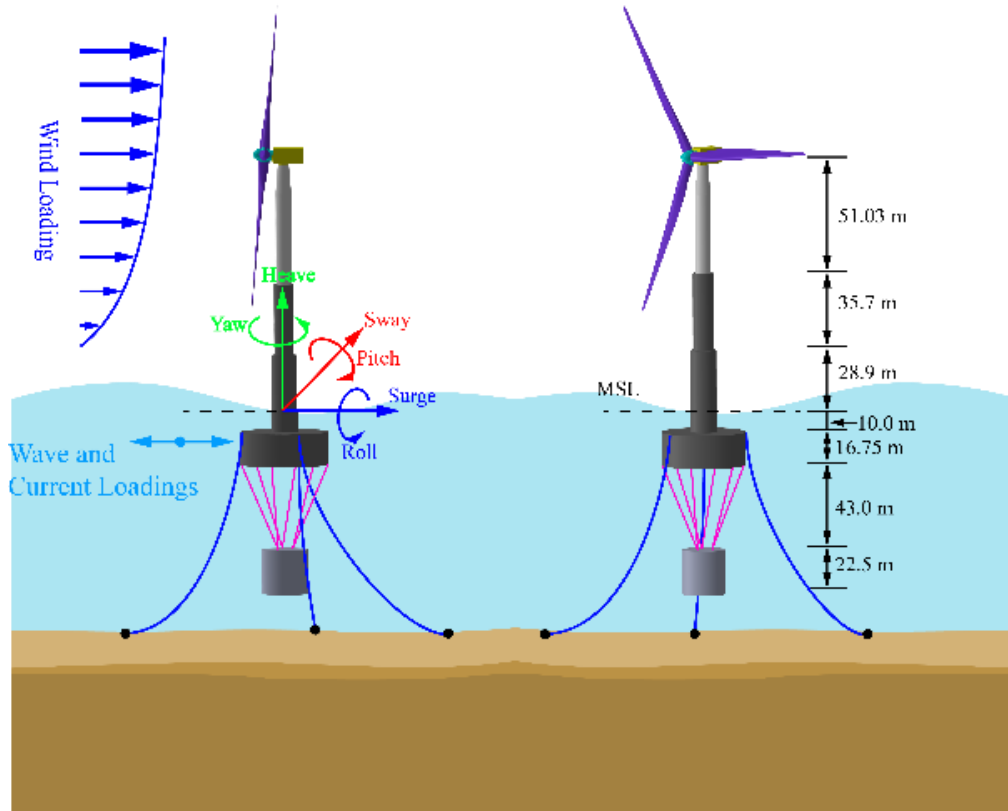

Fig.2: The 10 MW multi-body wind turbine

Fig. 3 presents the orientations of the tendons and mooring lines. There are 6 and 3 connection points for the tendons on the UT and LT, respectively. The UT tendon connection points distribute uniformly around the circumference of the bottom surface. The fairleads of the mooring lines are attached on the top surface of the UT. Each of the mooring lines has an unstretched length of 620 m and a wet weight of 250 kg/m. The coordinates of the connection points of the tendons and mooring lines are presented in Table 2.
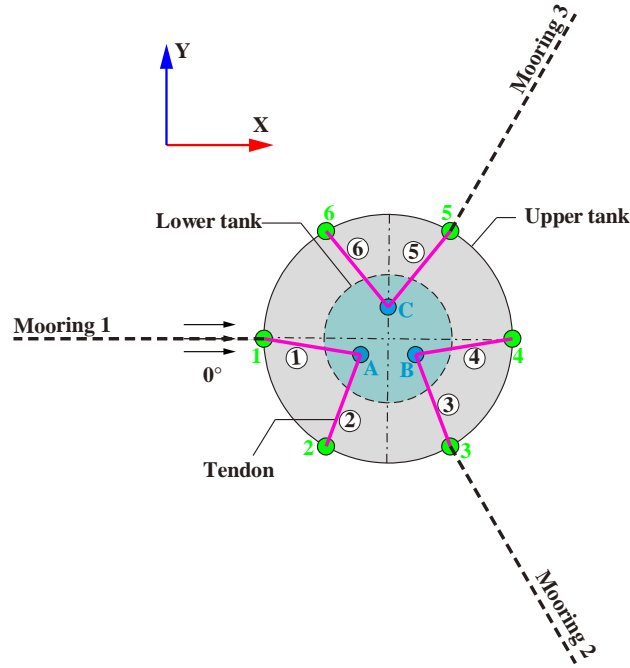
Fig. 3: Orientations of the tendons and mooring lines

Table 2: Coordinates of connection points of tendons and mooring lines (referred to the MSL)

Connection points	x (m)	y (m)	z (m)
UT 1	11.13	19.27	-26.75
UT 2	-11.13	19.27	-26.75
UT 3	-22.25	0.00	-26.75
UT 4	-11.13	-19.27	-26.75
UT 5	11.13	-19.27	-26.75
UT 6	22.25	0.00	-26.75
LT A	0.00	4.51	-67.50
LT B	-3.90	-2.25	-67.50
LT C	3.90	-2.25	-67.50
Fairlead 1	11.13	19.27	-10.00
Fairlead 2	-22.25	0.00	-10.00
Fairlead 3	11.13	-19.27	-10.00
Anchor 1	300.00	519.62	-110.00
Anchor 2	-600.00	0.00	-110.00
Anchor 3	300.00	-519.62	-110.00

By conducting free decay analysis of the moored FWT in all six degrees of freedom, natural periods and frequencies of the platform in the six degrees of freedom (DOFs) are obtained and presented in Table 3.

Table 3: Natural periods and frequencies of the platform

	Surge	Sway	Heave	Roll	Pitch	Yaw

Period/(s)	322.8	322.7	52.7	36.3	36.3	115.6
Frequency/(rad/s)	0.019	0.019	0.122	0.173	0.173	0.050

3. Coupling between AQWA and AeroDyn

3.1 Development of the coupling framework

FAST is an excellent multi-physical engineering tool that is commonly used for coupled analysis of FWTs. However, in its current form, FAST is incapable of examining the coupled effects of a multi-body platform connected by flexile elements, especially when the focus is the connection element. It is noted that AQWA is capable of performing frequency-domain and time-domain analyses of offshore and marine structures with multiple floaters. Although the baseline version of AQWA is not capable of calculating aerodynamic loads of FWTs, it accepts external forces calculated by a user-defined DLL at each time step of the time-domain analysis. Therefore, AQWA becomes a suitable option in this study as the numerical tool after modifying its built-in DLL to make it capable of handling servo-control and predicting aerodynamic loads of a multi-body FWT. Consequently, a coupling framework presented in Fig. 4 is developed and implemented by incorporating AeroDyn in AQWA after modifying its source code.

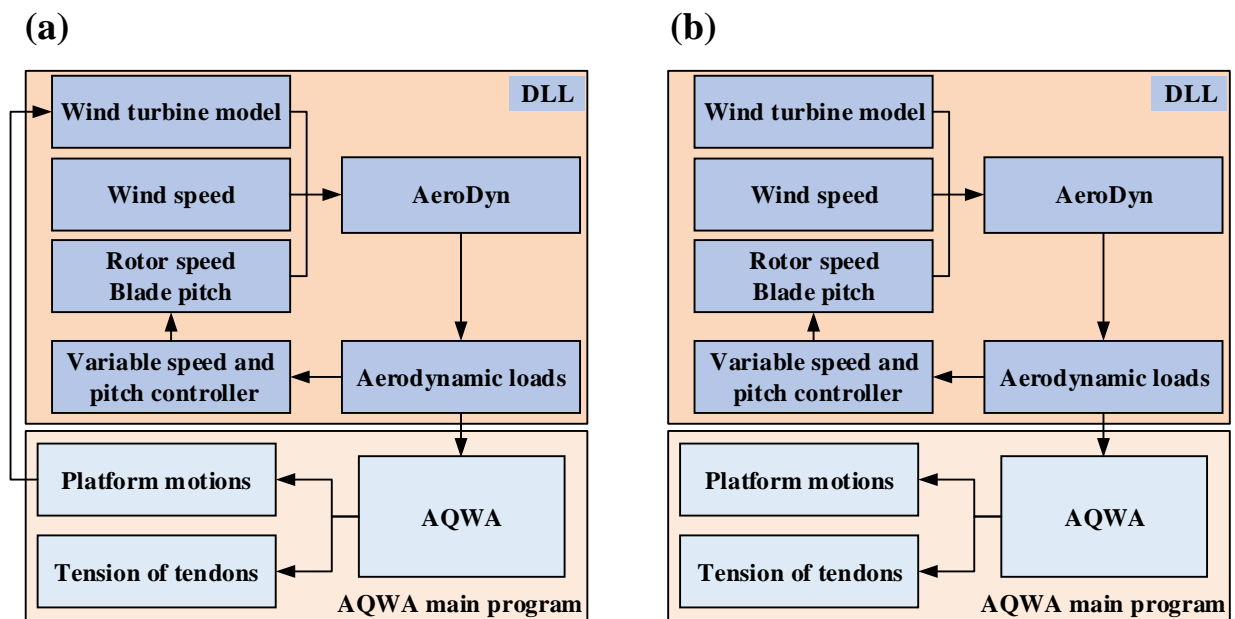**(a)**   **(b)**

Fig. 4: Flowcharts of (a) coupled model and (b) decoupled model based on AeroDyn and AQWA

The calculation procedure of the aerodynamic loads in every time step is coupled with the floating platform dynamic responses. To be more specifically, the relative speed between the rotor and inflow wind is affected by the platform surge and pitch rotation velocities. At each time step of the simulation in AQWA, the relative wind speed is calculated by:

$$V_{rel} = V_{in} - V_s - \omega_p \cdot (H_{hub} + h_{COG}) \tag{1}$$

where V_{rel} is the relative wind speed, V_{in} is the inflow wind speed, V_s and ω_p are the surge velocity and pitch velocity of the platform, respectively. H_{hub} is the hub height and h_{COG} is the distance of UT's CoG to the MSL.

In addition, a transformation matrix $\mathbf{T}_{mat}$ is applied to correct the rotor coordinates due to the platform rotational motions. The corrected coordinates (x, y, z) of a rotor point (x_0, y_0, z_0) is given as:

$$\begin{bmatrix} x \\ y \\ z \end{bmatrix} = \begin{bmatrix} \dfrac{\theta_1^2\sqrt{1+s}+\theta_2^2+\theta_3^2}{s\sqrt{1+s}} & \dfrac{\theta_3 s+\theta_1\theta_2(\sqrt{1+s}-1)}{s\sqrt{1+s}} & \dfrac{-\theta_2 s+\theta_1\theta_3(\sqrt{1+s}-1)}{s\sqrt{1+s}} \\ \dfrac{-\theta_3 s+\theta_1\theta_2(\sqrt{1+s}-1)}{s\sqrt{1+s}} & \dfrac{\theta_2^2\sqrt{1+s}+\theta_1^2+\theta_3^2}{s\sqrt{1+s}} & \dfrac{\theta_1 s+\theta_2\theta_3(\sqrt{1+s}-1)}{s\sqrt{1+s}} \\ \dfrac{\theta_2 s+\theta_1\theta_3(\sqrt{1+s}-1)}{s\sqrt{1+s}} & \dfrac{-\theta_1 s+\theta_2\theta_3(\sqrt{1+s}-1)}{s\sqrt{1+s}} & \dfrac{\theta_3^2\sqrt{1+s}+\theta_1^2+\theta_2^2}{s\sqrt{1+s}} \end{bmatrix} \begin{bmatrix} x_0 \\ y_0 \\ z_0 \end{bmatrix}$$

$$\tag{2}$$

where θ_1, θ_2 and θ_3 are the roll, pitch and yaw displacements of the platform, respectively; s is the sum of squares of each rotation equal to $\theta_1^2 + \theta_2^2 + \theta_3^2$.

During the time-domain simulation in AQWA, AeroDyn is invoked at each time step to calculate aerodynamic loads of the wind turbine based on the operational parameters including the rotor speed, blade pitch, tilt angle and yaw angle. The generalized dynamic wake model (GDW) is used to examine the dynamic inflow effects of the wind turbine. The force vector

obtained by AeroDyn through the DLL is applied at the hub height of the wind turbine. The dynamic responses of the platform subjected to the coupled loadings at the next time step are then calculated in AQWA. The equation of motion of each of the UT and LT is given below:

$$(\boldsymbol{m} + \boldsymbol{A}_{\mathrm{wv}})\ddot{\boldsymbol{X}}(t) + \boldsymbol{C}\dot{\boldsymbol{X}}(t) + \boldsymbol{K}\boldsymbol{X}(t) + \int_0^t \boldsymbol{h}(t-\tau)\ddot{\boldsymbol{X}}(\tau)\mathrm{d}\tau = \boldsymbol{F}_{\mathrm{h}}(t) + \boldsymbol{F}_{\mathrm{t}}(t) + \boldsymbol{F}_{\mathrm{e}}(t) \qquad (3)$$

where $\boldsymbol{m}$ is the inertial mass matrix of the platform, $\boldsymbol{A}_{\mathrm{wv}}$ is the hydrodynamic added-mass matrix; $\boldsymbol{K}$ and $\boldsymbol{C}$ are, respectively, the total stiffness and damping matrices; $\boldsymbol{X}(t)$, $\dot{\boldsymbol{X}}(t)$ and $\ddot{\boldsymbol{X}}(t)$ are, respectively, the displacement, velocity and acceleration vectors of the platform; $\boldsymbol{h}(t)$ is the impulse function matrix used to examine the hydrodynamic radiation memory effects as denoted in Eq. (4); $\boldsymbol{F}_{\mathrm{h}}(t)$ and $\boldsymbol{F}_{\mathrm{t}}(t)$ are, respectively, the hydrodynamic and mooring load vectors acting on the platform; $\boldsymbol{F}_{\mathrm{e}}(t)$ is the external force vector obtained through the DLL.

$$\boldsymbol{h}(t) = \frac{2}{\pi}\int_0^\infty \boldsymbol{B}(\omega)\frac{\sin(\omega t)}{\omega}\mathrm{d}\omega \qquad (4)$$

where $\boldsymbol{B}(\omega)$ is the radiation damping and ω is the wave frequency.

The added mass, radiation damping and excitation forces of both the UT and LT are calculated in AQWA by performing a frequency domain analysis based on the potential theory. Each mooring line is modelled as a dynamic catenary. The inertial effects of the mooring line and the platform motions are considered in predicting the mooring tensions. It is noted that the external force of the LT is zero while the external force acting on the UT is calculated using the DLL. The aerodynamic loads acting on the hub obtained through the DLL are referenced to the UT's local coordinate system, and the external force item in Eq. (3) is applied at the UT's centre of mass and referenced to the inertial coordinate system. Therefore, aerodynamic loads directly obtained through the DLL are converted using Eq. (5) and Eq. (6) before being passed into the AQWA solver for solving the equation of motion.

$$\mathbf{F}_{\text{AQWA}} = \mathbf{T}_{\text{mat}}^{-1} \cdot \mathbf{F}_{\text{DLL}} \tag{5}$$

$$\mathbf{M}_{\text{AQWA}} = \mathbf{T}_{\text{mat}}^{-1} \cdot \left[\mathbf{M}_{\text{DLL}} + (\mathbf{Hub\text{-}CoG}) \times \mathbf{F}_{\text{DLL}} \right] \tag{6}$$

where $\mathbf{F}_{\text{AQWA}}$ and $\mathbf{F}_{\text{DLL}}$ are the translational force vectors in the AQWA solver and DLL, respectively. $\mathbf{T}_{\text{mat}}^{-1}$ is the inverse matrix of $\mathbf{T}_{\text{mat}}$. $\mathbf{M}_{\text{AQWA}}$ used in AQWA is the moment vector acting at the UT's centre of mass with respect to the inertial coordinate system. $\mathbf{M}_{\text{DLL}}$ obtained in the DLL is the moment vector acting at the hub-height with respect to the platform's local coordinate system. $\mathbf{Hub}$ and $\mathbf{CoG}$ are the position vectors of the hub and the UT, respectively.

3.2 Implementation of the torque-pitch controller

In order to examine the start-up procedure and normal power production cases, a torque-pitch controller is developed and integrated with the AQWA-AeroDyn coupling interface to adjust the rotor speed and blade pitch. The torque-pitch controller consists of a simple partial-load controller and a proportional-integral (PI) controller. The partial-load controller defines the relationship between desired torque and speed of the generator when the output power is smaller than the rated power. The PI controller takes over to adjust blade pitch once the output power exceeds the rated power. Referring to the basic algorithm applied for a 5 MW wind turbine [24], the torque-speed variation is divided into 5 regions as shown in Fig. 5.
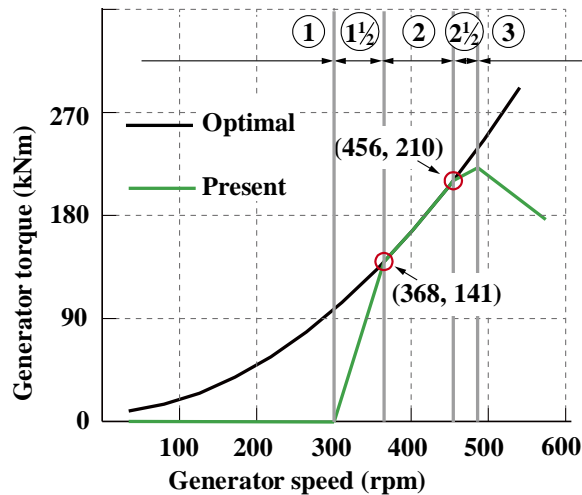

Fig. 5: Torque versus speed of the controller

Region 1 corresponds to the start-up process of the wind turbine. The generator torque remains 0 until the rotor speed exceeds the minimum speed (6.0 rpm). Region 1½ is a transitional region where the generator will be accelerated to reach the minimum speed at region 2 that is the control region with an optimal efficiency to capture wind energy as the wind turbine operates under the best tip speed ratio (TSR). The generator torque is proportional to the square of the generator speed in this region. Region 2½ is used to limit the minimum generator speed at rated power and the maximum blade tip speed due to noise emission. In region 3, the wind turbine outputs the rated power constantly, implying that the generator speed is inverse to the torque.

For the DTU 10 MW wind turbine, the minimum rotor speed is 6.0 rpm and the gearbox ratio is 50, implying that the starting limit of region $1½$ is 300.0 rpm. The starting and ending limits of region 2 are chosen as 123% of the minimum generator speed and 95% of the rated generator speed, respectively. By assuming that the generator power at 480 rpm is 10 MW with an efficiency of 94.4% [24], generator torques corresponding to 368 rpm and 456 rpm are 141 kN·m and 210 kN·m, respectively. In order to avoid excessive overloading in region 3, the saturated torque is set as 10% above the rated capacity and the maximum torque ratio is 75 kN·m/s.

In region 3, the pitch controller is activated to adjust blade pitch angle for moderating structural loads and cutting off excess power. The adjustment of blade pitch is determined by aerodynamic power which is influenced by rotor speed. Therefore, the pitch control is implemented through the developed PI model of rotor speed and blade pitch. The drivetrain system which consists of the rotor and the generator can be treated as a single DOF system. The equation of motion of the drivetrain system is denoted as:

$$T_r - N_g T_g = (I_r + N_g^2 I_g)\frac{\mathrm{d}(\Omega_0 + \Delta\Omega)}{\mathrm{d}t} = I_{gt}\Delta\dot{\Omega} \tag{7}$$

where T_r is rotor torque and T_g is generator torque. N_g is gearbox ratio; I_r and I_g are the rotor inertia and generator inertia, respectively. Ω_0 and $\Delta\Omega$ are the rated rotor speed and rotor speed perturbation during $\mathrm{d}t$, respectively. I_{gt} is the drivetrain inertia and $\Delta\dot{\Omega}$ is rotor acceleration perturbation.

The blade pitch error $\Delta\theta$ can be denoted in a PI form as:

$$\Delta\theta = K_P N_g \Delta\Omega + K_I \int_0^t N_g \Delta\Omega \mathrm{d}t \tag{8}$$

where K_P and K_I are the proportional gain and integral gain, respectively, which are denoted as:

$$K_P = \frac{2I_{gt}\Omega_0 \xi_\varphi \omega_{\varphi n}}{N_g(-\partial P/\partial\theta)} \tag{9}$$

$$K_I = \frac{I_{gt}\Omega_0 \omega_{\varphi n}^2}{N_g(-\partial P/\partial\theta)} \tag{10}$$

where $\omega_{\varphi n}$ and ξ_φ are the frequency and damping ratio of the controller.

The frequency and damping ratio of the basic pitch controller developed by DTU for the 10 MW reference wind turbine are 0.377 rad/s and 0.7, respectively [25]. By calculating the aerodynamic power at different blade pitch angles, the sensitivity of power to pitch $\partial P/\partial\theta$ can be obtained. As the $\partial P/\partial\theta$ varies considerably with blade pitch over region 3 [26], constant K_P and K_I are insufficient to adjust blade pitch effectively. Therefore, an adjustment coefficient $\eta(\theta)$ is used to correct K_P and K_I at different blade pitch angles:

$$K_{P\_\theta} = K_{P\_0} \cdot \eta(\theta) \tag{11}$$

$$K_{I\_\theta} = K_{I\_0} \cdot \eta(\theta) \tag{12}$$

where K_{P_θ} and K_{I_θ} are the proportional and integral gains at blade pitch θ, respectively. K_{P_0} and K_{I_0} are the proportional and integral gains at zero blade pitch, respectively.

As given in the DTU basic controller report, the PI gains at zero blade pitch are 0.010490 rad·s/rad and 0.002824 rad/rad, respectively [26]. The adjustment coefficient $\eta(\theta)$ is given as:

$$\eta=1\Big/\Big(1+\theta\big/\psi_1+\theta^2\big/\psi_2\Big) \tag{13}$$

where ψ_1 and ψ_2 are 3.46 rad and 0.21 rad^2, respectively.

The controller frequency is designed as 0.377 rad/s, which is larger than the roll/pitch natural frequency of the multi-body platform (see Table 3). In order to avoid potential resonant response of roll/pitch motion, the controller frequency is detuned by 4 times to 0.094 rad/s. The proportional and integral gains at zero blade pitch are 0.002622425 rad·s/rad and 0.00017654 rad/rad, respectively.

3.3 Validation of the AQWA-AeroDyn coupling framework

In order to validate the accuracy of the AQWA-AeroDyn coupling framework in predicting the aero-hydro-servo coupled responses of a FWT, a commonly-used numerical analysis tool, FAST, is employed for comparison purposes. In the comparisons between AQWA-AeroDyn and FAST, the DTU 10 MW wind turbine supported by the TELWIND platform is used. Since FAST is incapable of conducting simulations of a multi-body platform, the TELWIND platform is modelled as a unibody by assuming the tendons as rigid connections in both FAST and AQWA. The hydrodynamic coefficients including the added mass, radiation damping and excitation forces of the unibody platform required for the time domain analysis in FAST are calculated using AQWA.

The stiffness of the FWT tower used in this study is significantly higher than the DTU reference tower's. Consequently, the platform motions of the FWT, including and excluding the tower flexibility under a regular wave condition, are obtained using FAST in order to evaluate the effects of tower elasticity. The examined wave height and period are 1.80 m and 4.27 s, respectively. The current speed distribution along the water depth follows a power law profile with an exponent of 1/7 and the current speed at the MSL is 0.22 m/s. The average wind speed of the turbulent wind field at the hub height is 9 m/s. The statistical results are compared in Table 4. The measured platform motions of the rigid and flexible tower models are almost

identical. For instance, the relative difference between the maximum pitch motions of the rigid and flexible tower models is 0.908%. The difference between the mean surge, heave and pitch motions of the rigid and flexible towers are 0.019%, 0.024% and 0.898%, respectively, which are smaller than 1%. The difference in the standard deviations of the platform motions are also negligible. The comparison indicates that the platform motions of this particular FWT concept are not significantly affected by the tower flexibility. The plausible reason is that this large diameter tower is not necessarily flexible since the bending stiffness of the tower is very large. The tower base stiffness of this FWT is over 6 times larger than the stiffness of the DTU reference tower. In addition, the natural frequencies of the 1st-order and 2nd-order fore-aft bending modes of the tower are 0.46 Hz and 2.41 Hz, respectively, which are out of the excitation frequency range of the examined wave condition. As a result, the platform motions are insensitive to the tower elasticity for the examined wave condition.

Table 4: Statistical platform motions of the FWT including and excluding tower flexibility

		Surge (m)	Heave (m)	Pitch (deg)
Max	Rigid tower	48.820	9.694	4.802
	Flexible tower	48.780	9.694	4.846
	Difference	0.082%	0.000%	0.908%
Mean	Rigid tower	30.123	5.268	1.761
	Flexible tower	30.117	5.266	1.777
	Difference	0.019%	0.024%	0.898%
Standard deviation	Rigid tower	6.539	0.165	0.990
	Flexible tower	6.530	0.165	0.995
	Difference	0.147%	0.144%	0.521%

In order to ensure the consistency of the models in the validation between AQWA-AeroDyn and FAST, the tower and blades are modelled as rigid elements in the FAST simulation. A regular wave is used since the process of generating an irregular wave in AQWA and FAST is different. In order to confirm that the torque-pitch controller and AeroDyn have

been well integrated within AQWA, Fig. 6 presents the rotor thrust, generation power and rotor speed of the FWT predicted by FAST and AQWA-AeroDyn under the aforementioned loadings. It is observed that the rotor speed and generator power obtained using AQWA-AeroDyn are almost the same as the results calculated by FAST. It implies that the servo-control ability is well implemented within AQWA-AeroDyn for dynamic analysis of FWTs. Similarly, the rotor thrust predicted by AQWA-AeroDyn follows the same trend as the result of FAST. The difference in magnitude between the results calculated in these two tools is negligible. This indicates that AeroDyn has been well integrated with AQWA for performing aero-hydro-servo analysis of FWTs.
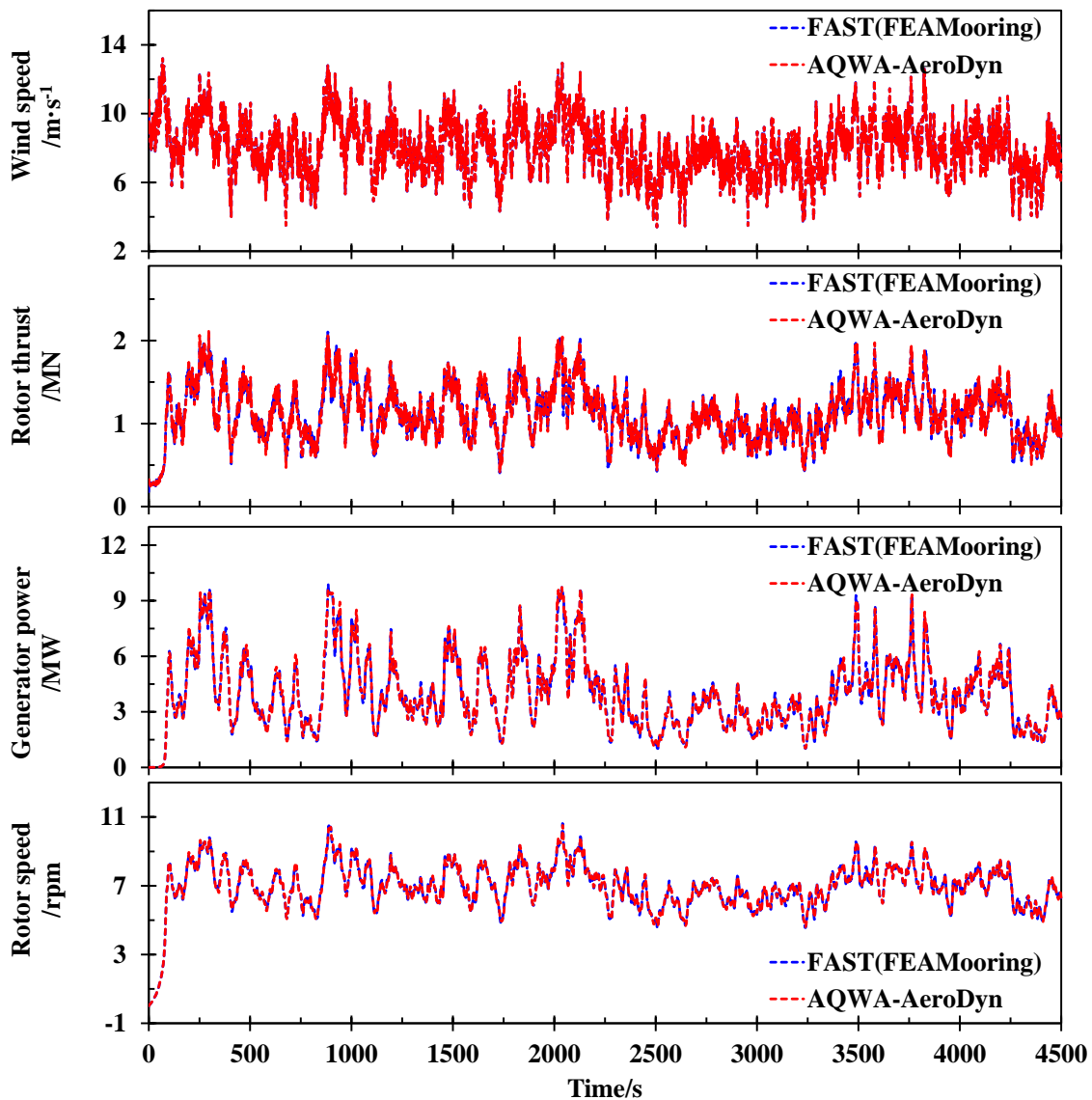
Fig. 6: Rotor thrust, generator power and rotor speed of the FWT predicted by FAST and

AQWA-AeroDyn

The coupled platform responses due to the wind-wave-current loadings are calculated by AQWA-AeroDyn and FAST and then compared in Fig. 7. In the simulation performed using FAST, the FEAMooring module is adopted to examine the dynamics of mooring lines. It can be seen that the platform surge from AQWA-AeroDyn follows the same variation trend as the results of FAST over the entire simulation. The platform surge motions predicted by these two tools fluctuate within a similar range, although slight differences are observed before the completion of the transient behaviour. The average surge motions (between 1500 s to 4500 s) predicted by FAST and AQWA-AeroDyn are 29.0 m and 29.8 m, respectively. The corresponding standard deviations are 6.93 m and 7.14 m, respectively, meaning that the relative error is around 3.0 %. Although both AQWA and the FEAMooring module in FAST employ the finite element method to examine the dynamics of the mooring lines, a slight difference exists in their implementations. In FEAMooring, the hydrodynamic loads acting on the mooring lines are calculated based on the wave kinematics of their initial positions [27]. However, AQWA calculates the hydrodynamic loads on the mooring lines based on the wave kinematics of their actual positions. In addition, the slight differences between the surge motions from these two tools are also caused by the hydrodynamic loads of the platform. As required by HydroDyn, which is the FAST module for calculating the hydrodynamic loads, the vertical centre of mass of the platform is set to zero when performing the frequency domain analysis needed to obtain the added mass, radiation damping and excitation forces. This is done to avoid double counting of the pitch and roll restoring forces that are intrinsically considered in the ElastDyn module of FAST if the centre of mass of the platform is set appropriately [28]. Consequently, the excitation pitch force is smaller compared to the realistic excitation force

that is obtained by setting the actual centre of mass of the platform when performing the frequency domain analysis. Nonetheless, the overall agreement between the platform surge responses from AQWA-AeroDyn and FAST is good.

Better agreements between AQWA-AeroDyn and FAST are observed in the predictions of the platform heave and pitch motions. The platform heave calculated by AQWA-AeroDyn follows the same variation trend as the results predicted using FAST, since the fluctuation of vertical load on the platform is small. The AQWA-AeroDyn slightly overestimates the heave response and this is attributed to the difference between the heave restoring forces of the mooring lines of AQWA and FAST. The platform pitch motion obtained using AQWA-AeroDyn agrees very well with the results of FAST in terms of both magnitude and trends, although negligible discrepancies exist.
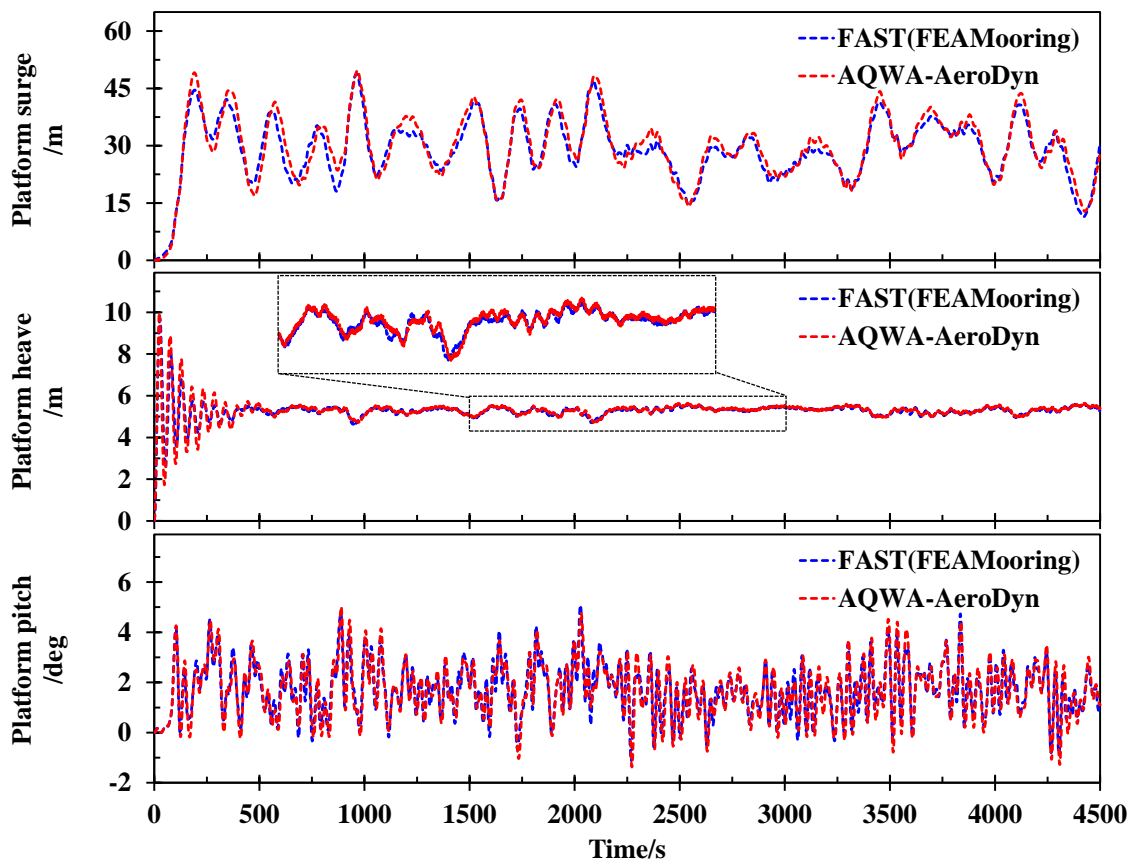
Fig. 7: Comparison of platform motions of the FWT predicted by FAST and AQWA-AeroDyn

The spectral responses of the platform motions are obtained and presented in Fig. 8 by applying the Fast Flourier Transformation (FFT) on the time series (from 1500 s to 4500 s). The spectral amplitude of the surge motion calculated by AQWA-AeroDyn agrees well with FAST's result at the natural frequency of surge mode. The heave amplitudes calculated by these two tools follow the same trend versus frequency, although AQWA-AeroDyn obtains slightly larger predictions. The overall discrepancy in the magnitude is small. The agreement between the two numerical analysis tools in predicting the pitch motion is good. The results have a similar spectral amplitude at the natural frequency of the pitch mode.
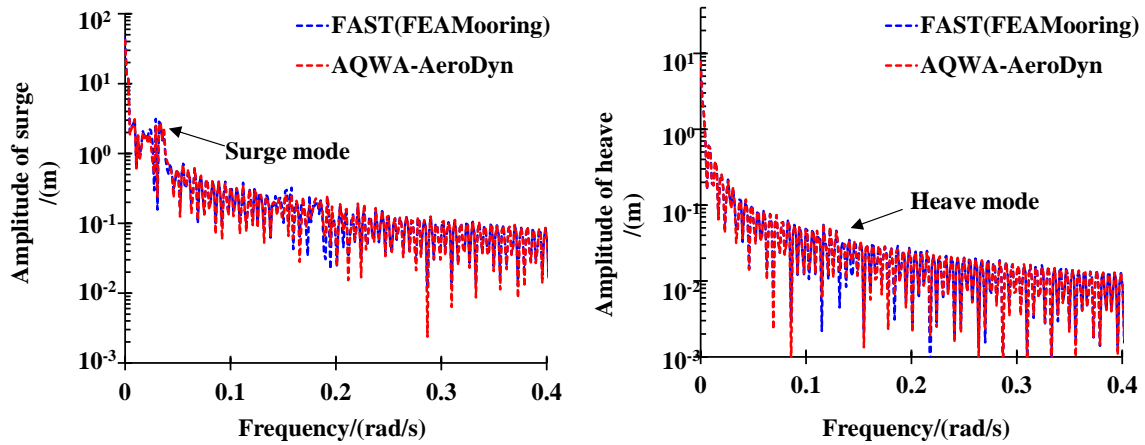
(a) Surge

(b) Heave
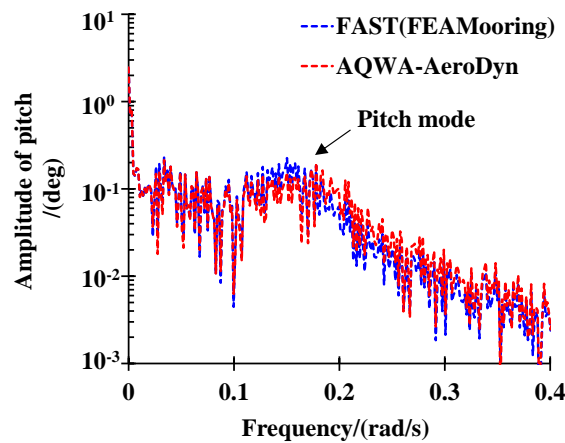
(c) Pitch

Fig. 8: Comparison of spectral responses of the platform calculated using FAST and AQWA-

AeroDyn

The comparisons against FAST have verified the accuracy and credibility of AQWA-AeroDyn in predicting aero-hydro-servo coupled responses of FWTs, although some discrepancies in the surge motion are observed. The overall agreements between AQWA-AeroDyn and FAST are reasonably good for aerodynamic load calculation and servo-control. In addition, the discrepancies in platform heave and pitch motions between the results obtained using these two tools are small. The comparisons indicate that the developed AQWA-AeroDyn coupling framework can be used to perform dynamic analysis of the 10 MW FWT supported by the TELWIND multi-body platform subjected to wind, wave and current loadings.

4. Evaluation of fatigue damage

The fluctuating tensions obtained from AQWA-AeroDyn are broken down into individual hysteresis cycles using the rainflow counting approach. The fatigue damage is assumed to accumulate linearly with each of the load cycles according to Miner's rule, as denoted by Eq. (14):

$$D = \sum_i \frac{n_i}{N_i(L_{i,RF})} \tag{14}$$

where D is total fatigue damage, n_i is the cycle count of the ith time series, N_i is the number of cycles to failure due to the cycle load range $L_{i,RF}$ over a fixed load-mean value. According to a *S-N* curve, N_i can be denoted as follows:

$$N_i = \left(\frac{L_{ult} - |L_{mf}|}{0.5L_{i,RF}} \right)^m \tag{15}$$

where L_{ult} is the ultimate design load of the tendon. L_{mf} denotes the fixed load-mean which is calculated by aggregating all of the time series of the load cases. *m* is the Wöhler exponent. In

accordance with the specification of the IEC standard [23] for steel strands, the selected S-N curve has a stress of 320 MPa corresponding to 5×10^5 cycles and a stress of 250 MPa at 2×10^6 cycles, resulting in a Wöhler exponent of 6.

In an actual situation, load cycles occur over a spectrum of mean loads rather than a fixed mean load. Therefore, the Goodman correction is applied to adjust the cycle load range $L_{i,RF}$ as shown in Eq. (16):

$$L_{i,RF} = L_{i,R}\left(\frac{L_{ult} - \left|L_{mf}\right|}{L_{ult} - \left|L_{i,M}\right|}\right) \tag{16}$$

where $L_{i,R}$ is the ith cycle range over the load-mean $L_{i,M}$.

Fig. 9 presents the process of the fatigue evaluation.
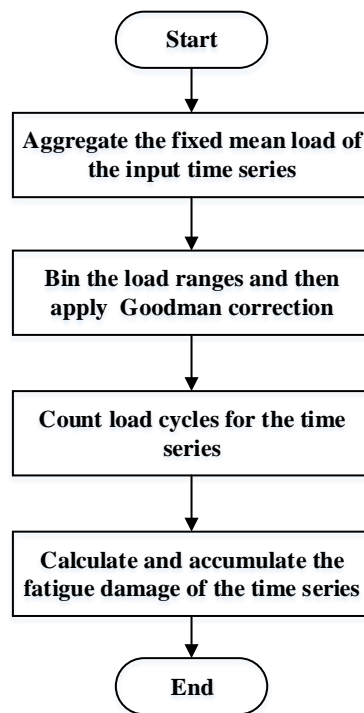
Fig. 9: The process of fatigue evaluation

5. Design load cases

A site of the floating wind farm located at the northern coast of Scotland as shown in Fig. 10 is examined. Based on the met-ocean data observed from 2011 to 2016 [29], the probability of a wind speed associated with the significant wave height and peak spectral period is obtained.

Fig. 11 presents the probability of the wind speed distribution for the specific site. It is noted that the wind speed is referred to the hub height and a power law profile with an exponent of 0.12 is used for calculating the wind speed based on the observed data at 10 m above the MSL.

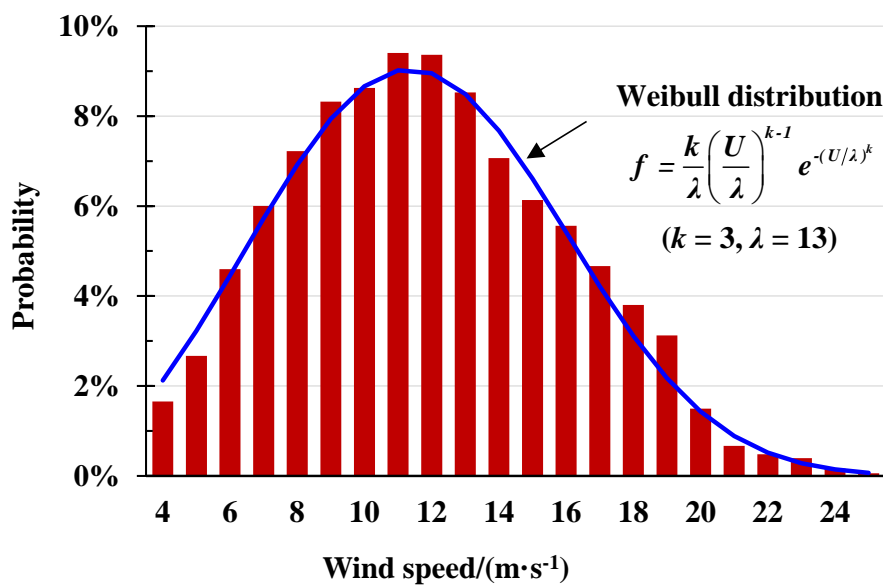Fig. 10: The specific site off the northern coast of Scotland

Fig. 11: Probability of the wind speed distribution of the specific site

Based on the observed met-ocean data provided by Ifremer [29], the wave heights and periods corresponding to the defined wind speeds are obtained. In addition, the current speed distribution along the water depth follows a power law profile with an exponent of 1/7 and the

current speed at the MSL is 0.22 m/s for each of the load cases. The inflow directions of the wind, wave and current are 0 degree (see Fig. 3). Table 5 presents the load cases defined for the fatigue analysis.

Table 5: Load cases for the fatigue analysis

Wind speed (m/s)	Significant wave height (m)	Peak spectral period (s)	Probability (-)
4.0	1.6146	3.4985	1.654%
5.0	1.6356	3.5989	2.670%
6.0	1.6660	3.7746	4.599%
7.0	1.6987	3.9842	6.003%
8.0	1.8037	4.2657	7.220%
9.0	1.9027	4.6698	8.322%
10.0	2.0125	4.8954	8.624%
11.0	2.1155	5.2555	9.403%
12.0	2.2237	5.5570	9.361%
13.0	2.3660	5.9987	8.525%
14.0	2.4570	6.3366	7.065%
15.0	2.5570	6.5657	6.134%
16.0	2.6588	6.8895	5.563%
17.0	2.7985	6.9955	4.666%
18.0	2.9585	7.1203	3.800%
19.0	3.0125	7.2335	3.125%
20.0	3.1547	7.4570	1.498%
21.0	3.3357	7.7785	0.667%
22.0	3.4587	8.0225	0.482%
23.0	3.6846	8.2266	0.397%
24.0	3.8975	8.5650	0.165%
25.0	4.0257	8.8897	0.058%

For both the coupled and decoupled analysis, the turbulent winds are generated using TurbSim [30] based on the Kaimal spectrum. A power law profile with an exponent of 0.12 is used to examine the wind-shear effect. The irregular waves are generated based on the Pierson-Moskowitz wave spectrum which can be found in [31].

6. Results and discussions

6.1 Wind-wave coupling effects on the platform motions

The multi-body platform is composed by two floating bodies (the UT and LT) which are connected by six tendons. In static conditions, the tendon tensions are the result of the difference of the weight and buoyancy between the UT and LT of the platform. The motion difference between the UT and LT affects the tension values of the tendons. Therefore, the fatigue damage of each tendon is significantly affected by the instant motion differences between the two tanks. Fig. 12 presents the motion differences between the UT and LT predicted using the coupled and decoupled methods under the condition with a wind speed of 15 m/s (see Table 5). It is noted that the first 1500 s of the analysis are truncated in order not to consider possible transient numerical analysis effects.
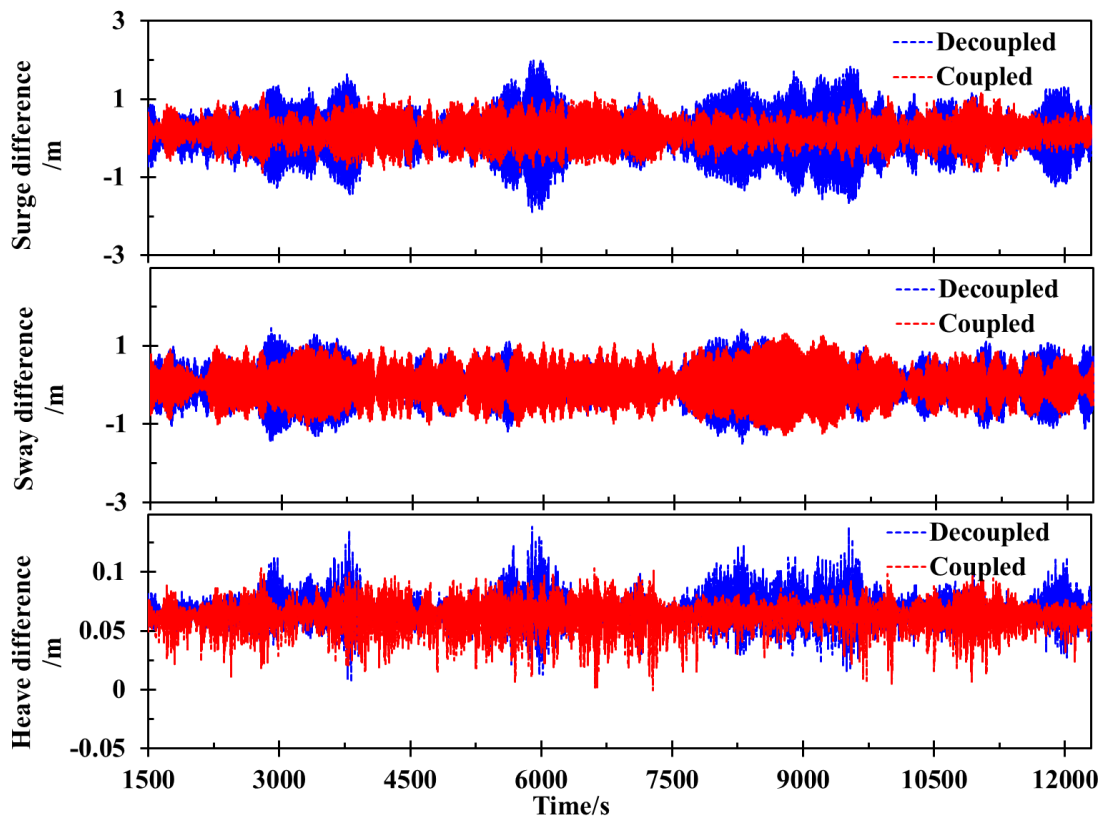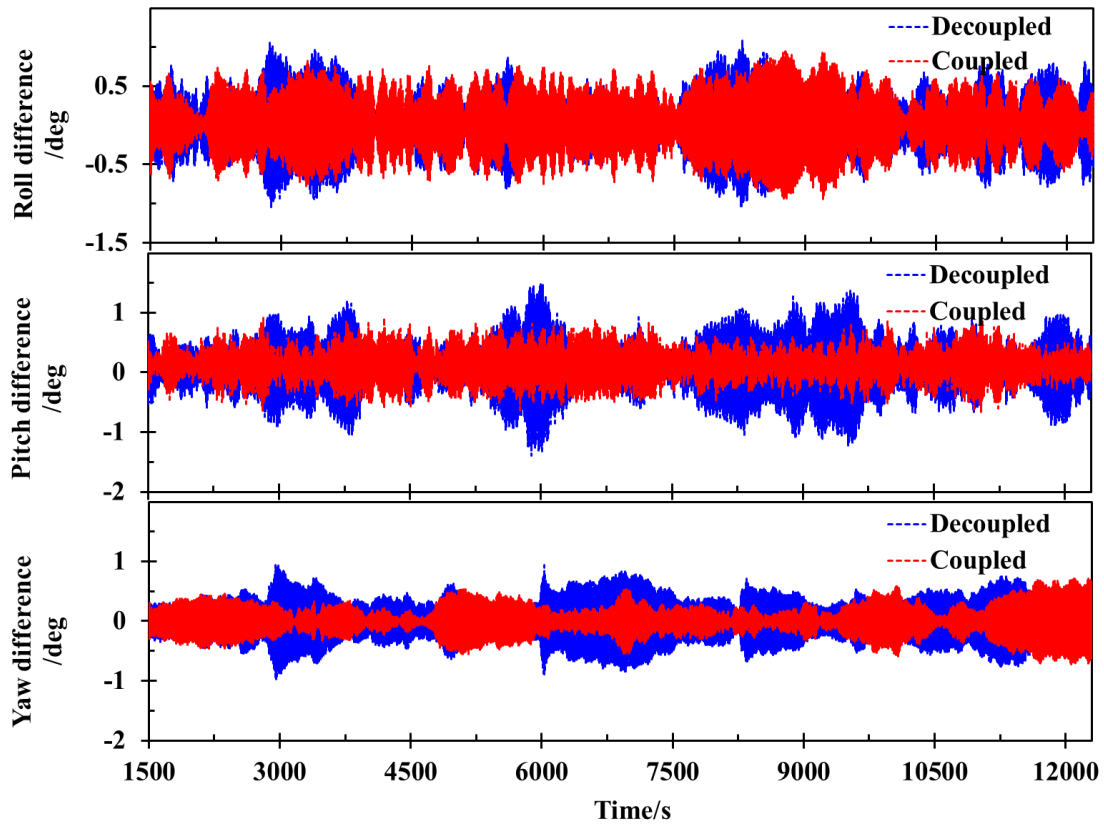
Fig. 12: Differences between the motions of the UT and LT predicted using the coupled and decoupled methods under the condition with a wind speed of 15 m/s

The motion differences between the two tanks obtained using the coupled model are smaller than the relevant differences obtained with the decoupled model for all six DOFs. The discrepancies in the surge, pitch and yaw motions between the results predicted using the coupled and decoupled models are relatively larger when compared with the ones in other three motions. The surge, pitch and yaw motions are more sensitive to the coupling between aerodynamic and hydrodynamic loads. The statistics of the motion differences are presented in Table 6. It is noted that the maximum surge difference obtained from the coupled analysis is 1.245 m, while the corresponding value predicted using the decoupled method is 2.134 m, resulting in a 71% overestimation. In addition, the standard deviation of the surge difference obtained using the decoupled and coupled models are 0.609 m and 0.358 m, respectively. It implies that an overestimation of 70% is made on surge difference if the coupling effect between aerodynamic loads and platform responses is ignored. Similar discrepancy between

the results calculated using the coupled and decoupled methods is observed for the pitch motion. The standard deviations of the motion differences are overestimated by the decoupled model. It is anticipated that the tension of each tendon predicted by the decoupled method would have a larger magnitude and more severe fluctuation compared to the one obtained from the coupled method, as the tensions in the tendons are significantly affected by the relative position of the two tanks.

Table 6: Statistics of the differences between the motions of the UT and LT

Statistics	Model	Surge (m)	Sway (m)	Heave (m)	Roll (deg)	Pitch (deg)	Yaw (deg)
Maximum	Coupled	1.245	1.335	0.107	0.984	0.954	0.753
	Decoupled	**2.134**	1.536	0.141	1.120	**1.585**	0.977
Standard deviation	Coupled	0.358	0.497	0.013	0.366	0.267	0.230
	Decoupled	**0.609**	0.500	0.012	0.367	**0.448**	0.327
Mean	Coupled	0.151	0.008	0.062	0.011	0.124	-0.001
	Decoupled	0.083	-0.012	0.067	0.009	0.068	-0.001

6.2 Wind-wave coupling effects on the tendon tension

The time-varying tensions of the six tendons under the condition with a wind speed of 15 m/s are presented in Fig. 13. Table 7 presents the statistics of the tension of each tendon. Since the wind inflow direction is aligned with the orientations of tendon 1 and tendon 4, these two tendons suffer from the most severe tension as observed from the results of the decoupled model. It is noted that the tension of each tendon predicted by the decoupled model has a larger fluctuation magnitude compared to the results obtained using the coupled model. For instance, when comparing the results obtained using these two methods, there is an overestimation in the maximum tension in tendon 1 by around 28% resulting from neglecting the coupling effect. The standard deviation of the tension in tendon 1 predicted by the decoupled model is 57% larger than the relevant results of the coupled model. Similarly, the tension in tendon 4 obtained using the decoupled model is more severe than that obtained using the coupled model. The

maximum magnitude and standard deviation of the tension in tendon 4 is overestimated by 19% and 62%, respectively, due to the absence of coupling effects of hydrodynamic and aerodynamic loads. This implies that the coupling effect needs to be examined in the analysis of the tendons.
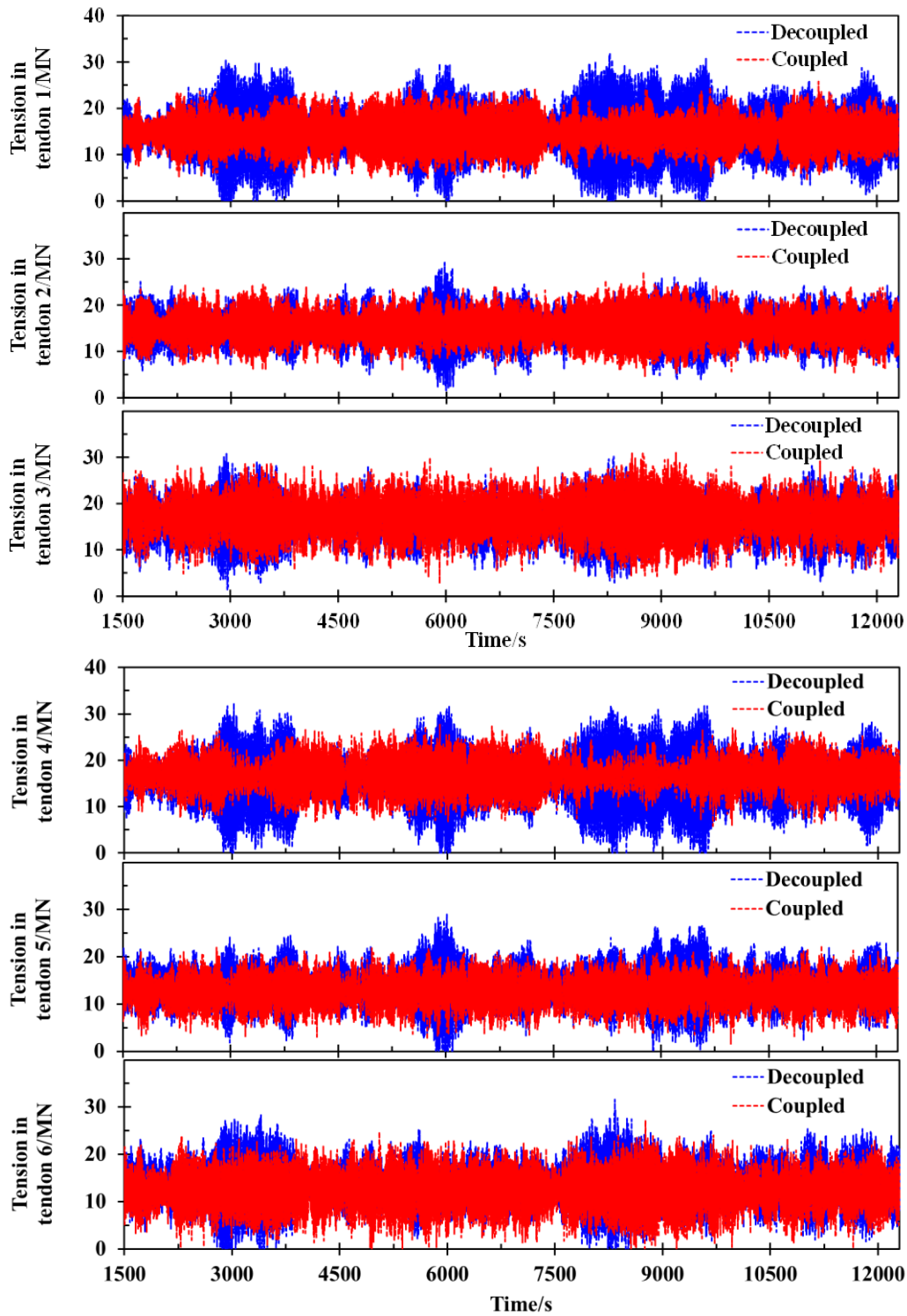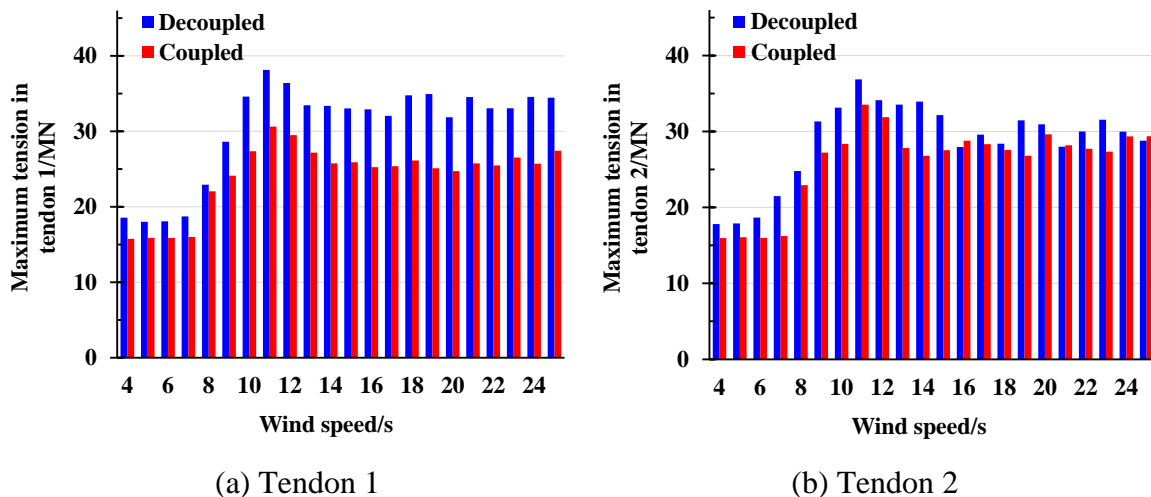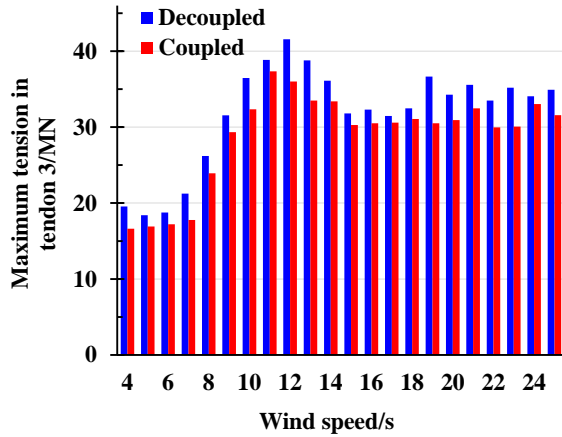

Fig. 13: The tension of each tendon under the condition with a wind speed of 15 m/s

Table 7: Statistics of the tension of each tension under the 15 m/s wind speed condition

Statistics	Model	Tendon 1 (MN)	Tendon 2 (MN)	Tendon 3 (MN)	Tendon 4 (MN)	Tendon 5 (MN)	Tendon 6 (MN)
Maximum	Coupled	25.90	27.54	32.71	28.03	22.75	27.15
	Decoupled	33.03	32.17	31.81	33.45	30.52	31.76
	Error	**28%**	17%	-3%	**19%**	34%	17%
Standard deviation	Coupled	3.68	3.50	4.48	3.51	3.39	4.45
	Decoupled	5.77	3.64	4.17	5.70	4.24	4.78
	Error	**57%**	4%	-7%	**62%**	25%	7%
Mean	Coupled	14.82	15.29	17.07	16.79	12.66	12.43
	Decoupled	14.90	15.12	16.01	15.88	13.63	13.54
	Error	1%	-1%	-6%	-5%	8%	9%

Fig. 14 presents the maximum tension of each tendon predicted by the coupled and decoupled models under the 22 load cases (defined in Table 5). It is observed that the tension in each tendon from the decoupled analysis is larger than the corresponding result obtained using the coupled model for each of the examined load cases. The absence of the coupling effects has a larger influence on the tension in tendon 1 and tendon 4 which are aligned with the wind direction. It implies that the coupling effects of platform responses and aerodynamic loads lead to a smaller discrepancy between the motions of the UT and LT, resulting in a smaller tension in the loading-aligned tendons.
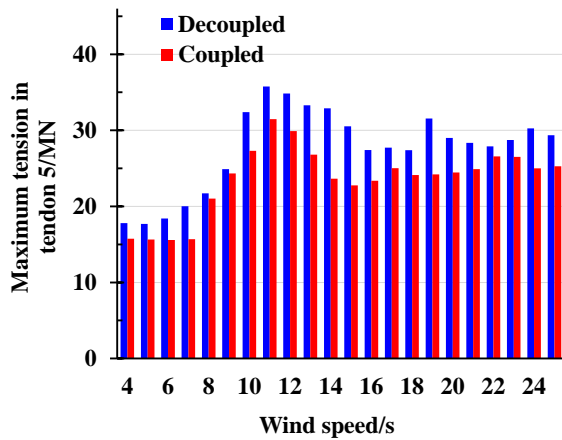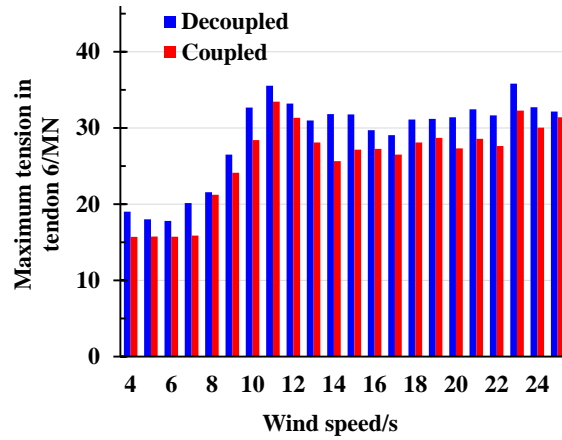

(a) Tendon 1
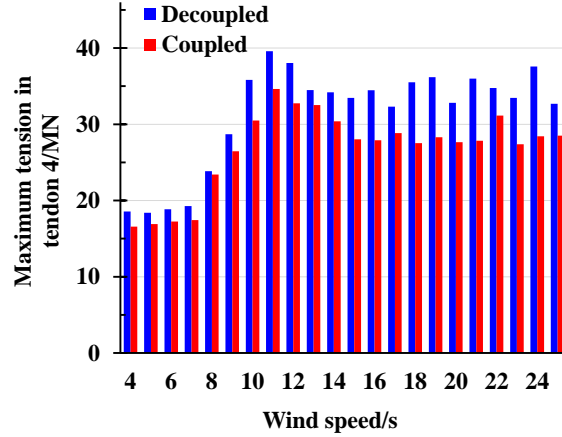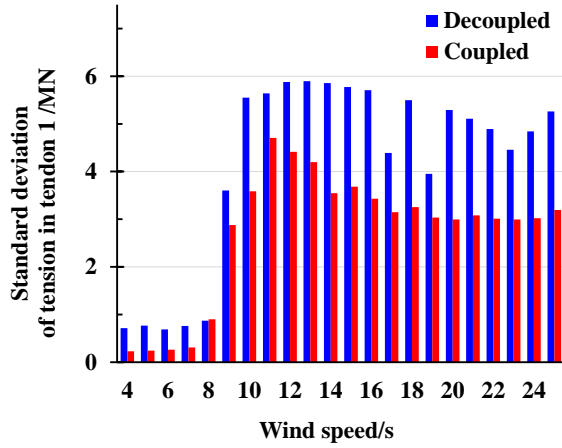
(b) Tendon 2

(c) Tendon 3
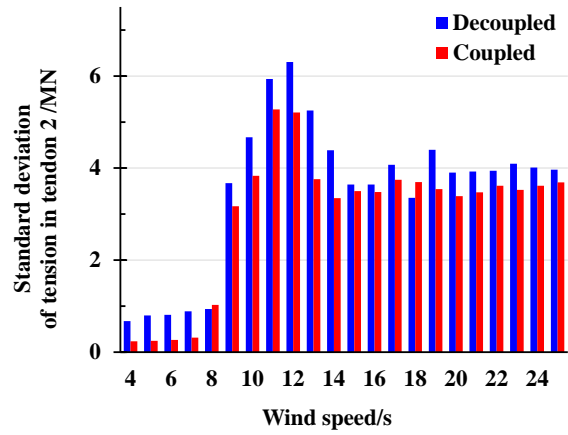
(d) Tendon 4

(e) Tendon 5

(f) Tendon 6

Fig. 14: Maximum tensions of each tendon under the 22 load cases

The standard deviations of the tension in each tendon obtained from the coupled and decoupled models are presented in Fig. 15. As can be seen, similar to the results of the maximum tension, the standard deviations of the tensions corresponding to the decoupled method are much larger than those of the coupled method. The maximum, mean and minimum overestimations are 227.3%, 43.7% and -17.1%, respectively, when the wind-wave coupling effects are ignored. This implies that the tension of the decoupled method fluctuates in a wider range. Consequently, the external loads produce larger fatigue damage to the tendons. It is anticipated that the fatigue damage predicted using the results from the decoupled method could be larger when compared to the results from the coupled method.
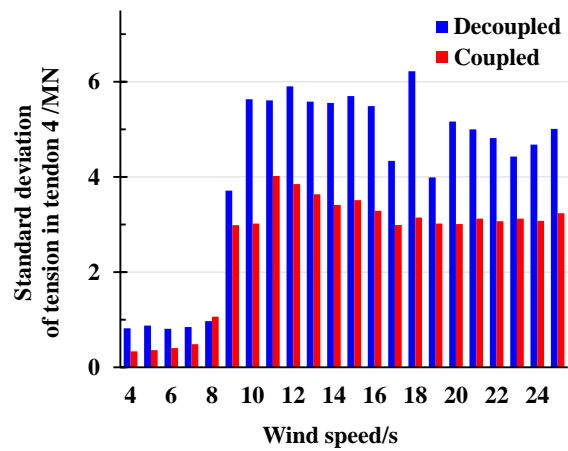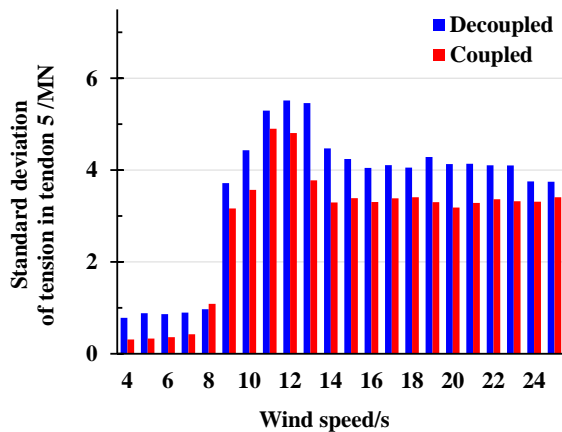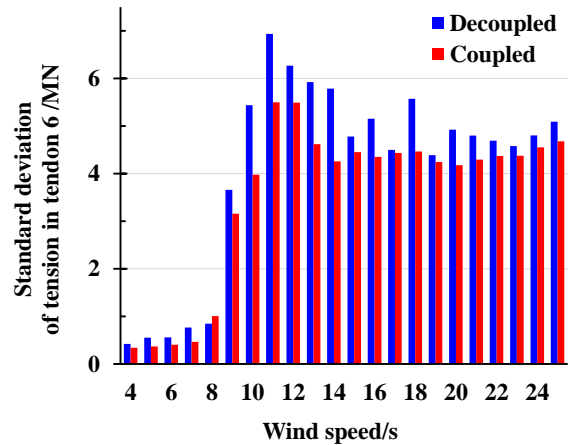
(a) Tendon 1

(b) Tendon 2
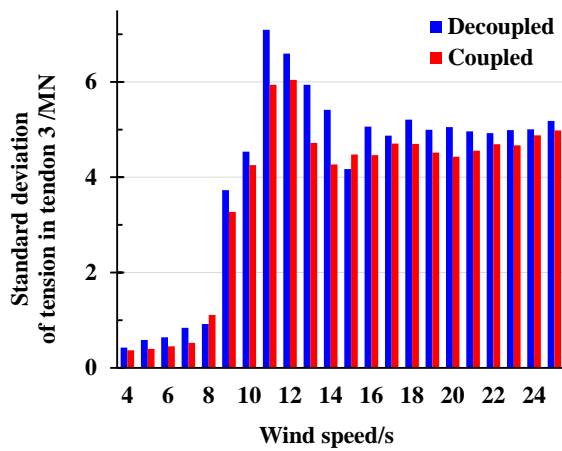
(c) Tendon 3

(d) Tendon 4
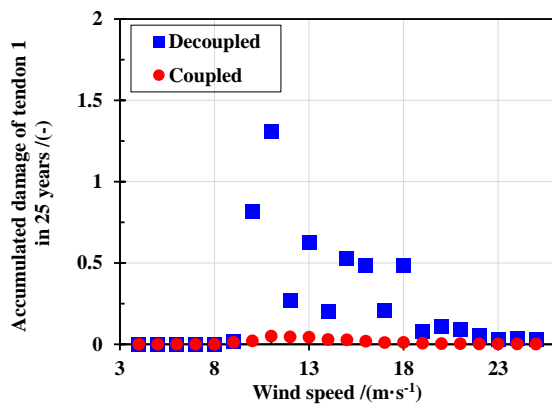
(e) Tendon 5

(f) Tendon 6

Fig. 15: Standard deviation of tension in each tendon under the 22 load cases

6.3 Fatigue damage assessment of the tendons

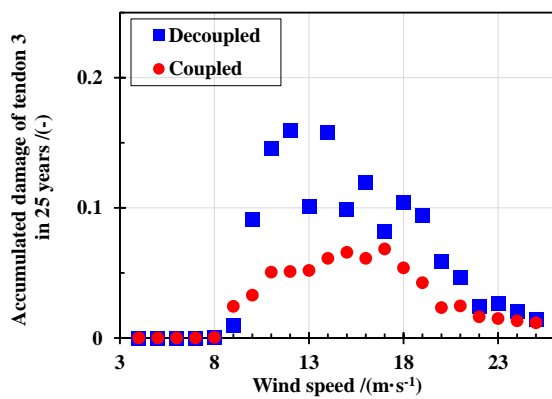### 6.3.1 Fatigue damage of the tendons

The fatigue damage of the tendons due to wind, wave and current loadings is evaluated based on the results obtained using the coupled and decoupled models. In order to avoid the impact of the transient behaviour on the platform when considering its low natural frequency, the first 1500 s of each time series are ignored in the fatigue damage evaluation. The accumulated fatigue damage in 25 years for each tendon based on the design load case is presented in Fig. 16. As can be seen, the decoupled method overestimates the fatigue damage by dozens of times for each examined case. More specifically, the accumulated fatigue damage of tendon 1 predicted by the coupled method is around 2.77×10^{-2} for the load case with a wind speed of 15 m/s, whereas the corresponding value of the decoupled method is 5.28×10^{-1} which is 19 times larger compared to the coupled method. This is mainly because the larger fluctuation range of the decoupled method causes more stress damage under the same load cycles. It further indicates that the coupling effect of wind and wave must be considered for a fatigue analysis.
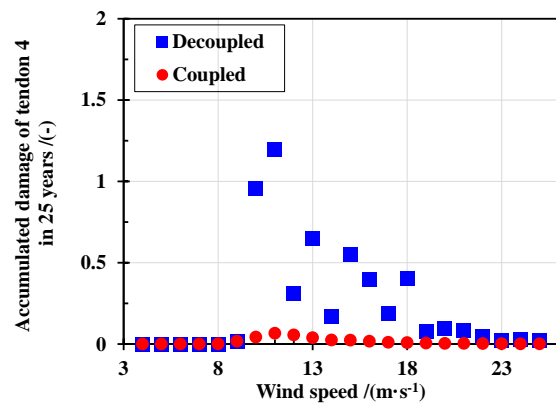

(a) Tendon 1

(b) Tendon 2

(c) Tendon 3

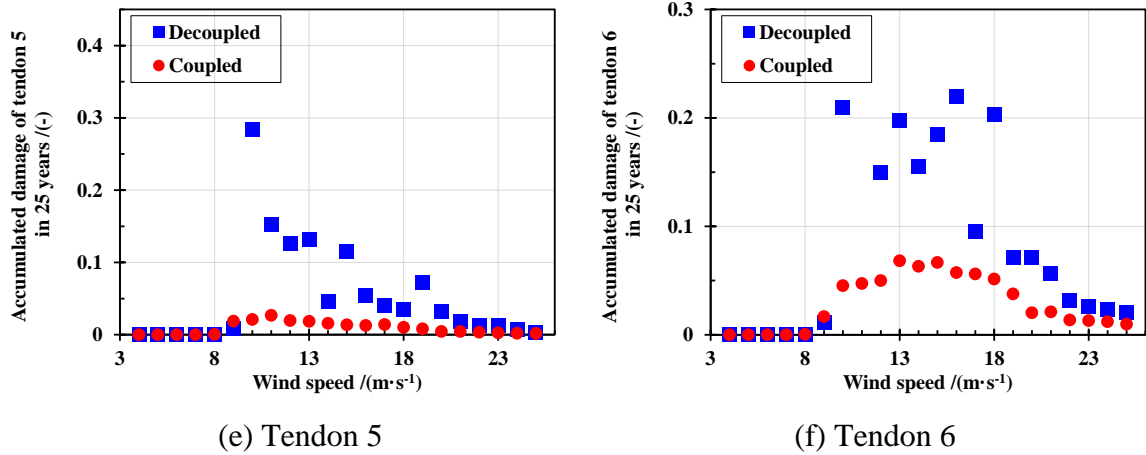(d) Tendon 4

(e) Tendon 5　　　　　　　　　　　　　(f) Tendon 6
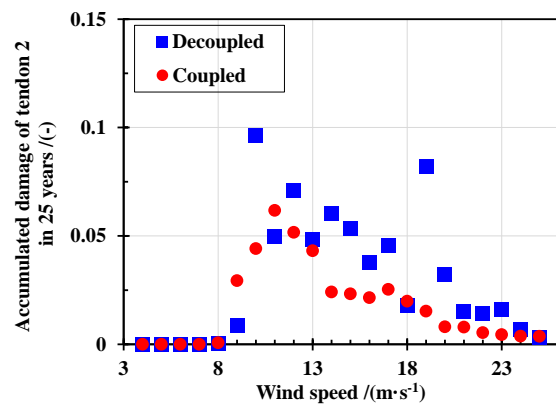
Fig. 16: Accumulated fatigue damage in 25 years the tendons under each examined case

The accumulated damage in 25 years and the lifetime of the tendons are presented in Table 8. As predicted using the results from the coupled method, all of the tendons are able to operate in the specific site for over 37 years. However, the fatigue evaluation using the results of the decoupled method is found to be too conservative. Fatigue damage would be overestimated by a factor of more than 15, leading to an unrealistic failure in tendon 1 and tendon 4 within 5 years due to fatigue. This comparison emphasizes that the coupling effect of wind and wave must be considered for the fatigue analysis of the DTU 10 MW reference wind turbine supported by the TELWIND multi-body platform due to the huge difference predicted.

Table 8: Accumulated fatigue damage in 25 years and lifetime of each tendon

		Tendon 1	Tendon 2	Tendon 3	Tendon 4	Tendon 5	Tendon 6
Fatigue damage (-)	Coupled	0.291	0.393	0.669	0.326	0.199	0.649
	Decoupled	5.363	0.659	1.355	5.218	1.154	2.144
Lifetime (years)	Coupled	85.88	63.54	37.36	76.73	125.44	38.53
	Decoupled	4.66	37.95	18.45	4.79	21.67	11.66

6.3.2 Influence of numerical simulation length

This particular FWT has large natural periods; hence the simulation length is suggested to be larger than 1 hour in order to cover every potential wave period and height [32]. It is noted that the examined wind turbine is subject to combined loadings of wind and wave. The

turbulent wind and irregular wave both have different magnitudes over the simulation. The effect of high ranges cannot be captured in short length simulations. This implies that simulation length may have a notable influence on the fatigue evaluation. However, the modelling of coupled environmental loadings for a FWT is a challenging work requiring significant computational resources for a fatigue analysis. For instance, this study conducted all the simulations at a workstation with 8 Intel Xeon 3.30 GHz cores, taking around 8 hours to complete one coupled simulation using AQWA incorporated with AeroDyn. In order to reduce the computational resource on the premise of accuracy of for the fatigue analysis, this study has calculated fatigue damages of the tendons for 7 different simulation lengths.

Fig. 17 presents the accumulated damages over 25 years of the tendons that are evaluated based on the results with different simulation lengths. For each of the examined simulation lengths, a 1500 s transient period is considered. In addition, the relative differences in the results of the 3-hours length are presented. As can be seen, significant difference is observed between the results of different effective simulation length analyses. More specifically, there is over 20% discrepancy between the 1-hour length and the 3-hour length for tendon 1. It implies that simulation length affects the accuracy of fatigue evaluation. As the effect of simulation length increases, the damages converges towards the result of the 3-hours length analysis. For the 6000 s length results, the relative differences in fatigue of 4 out of the 6 tendons are below 10% except for tendon 1 and tendon 4. For the 8400 s length results, the relative differences between the tendons are smaller than 10%. In this regard, around 20% computational resources can be saved.

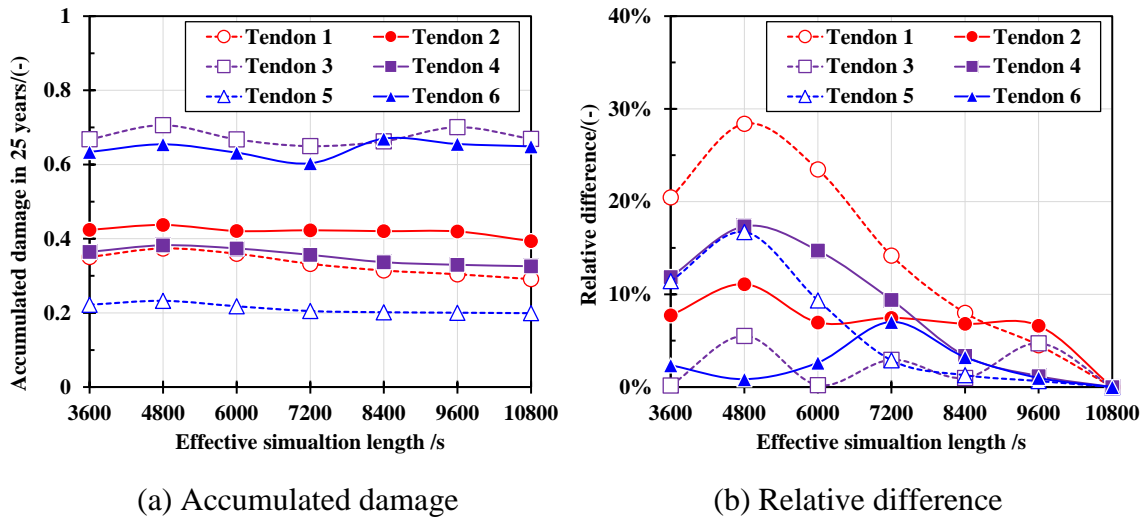(a) Accumulated damage   (b) Relative difference

Fig. 17: Accumulated damage in 25 years and lifetime of the tendons

7. Conclusions

This study presented a fatigue analysis of the tendons that connect the upper and lower tanks of a multi-body 10 MW FWT whose integrity determines the safety and stability of the platform. An aero-hydro-servo coupled analysis tool based on AQWA and AeroDyn is developed through a user-defined DLL to conduct numerical simulations of the FWT supported by a multi-body platform. The accuracy and credibility of the AQWA-AeroDyn coupling framework in predicting dynamic responses of the FWT is validated by comparing it with FAST. Based on the observed met-ocean data of the selected site at the northern coast of Scotland, 22 load cases are defined for a fatigue analysis. The dynamic responses of the FWT under each of the load cases are examined and compared using the coupled model and a decoupled model, respectively. The wind-wave coupling effects on the fatigue damage of each tendon is quantitatively evaluated based on the time-domain results of the coupled and decoupled methods. The results have confirmed the application feasibility of the TELWIND multi-body platform for supporting the DTU10 MW reference wind turbine. In addition, the influence of the effective simulation length on the fatigue damage is investigated and discussed. The main conclusions of this study are presented as follows:

- A generic aero-hydro-servo coupling tool is developed based on AQWA and AeroDyn. The agreement between the results obtained using the developed tool and FAST are reasonably good, indicating that a valid numerical tool capable of performing a wind-wave coupled analysis of a FWT supported by a multi-body platform has been developed.

- Neglecting the wind-wave coupling effect enhances the motion differences between the two tanks of the platform. Consequently, this increases the tension fluctuation in the tendons by 43%.

- The accumulated fatigue damage of each tendon during its design lifetime is overestimated by over 67% when the wind-wave coupling effects are not examined. It reduces the fatigue life estimation of each tendon by over 20 years from current design practice.

- The effective length of the simulations has a significant influence on the fatigue damage prediction. The simulation length must be longer than 8400 s for the fatigue analysis of the multi-body platform tendons to have an accuracy of more than 90% or an error that is less than 10%.

References

[1] GWEC. (2019). Global wind report 2018. *Global Wind Energy Council*, Brussels, Belgium.

[2] Wiser, R., Jenni, K., Seel, J., Baker, E., Hand, M., Lantz, E., & Smith, A. (2016). Expert elicitation survey on future wind energy costs. *Nature Energy*, 1(10), 1-8.

[3] Jonkman, J. (2010). Definition of the Floating System for Phase IV of OC3. *National Renewable Energy Laboratory (NREL), Technical Report No. NREL/TP-500-47535*, Colorado, United States.

[4] Karimirad, M., & Moan, T. (2011). Wave-and wind-induced dynamic response of a spar-type offshore wind turbine. *Journal of waterway, port, coastal, and ocean engineering*, 138(1), 9-20.

[5] Yu, M., Hu, Z. Q., & Xiao, L. F. (2015). Wind-wave induced dynamic response analysis for motions and mooring loads of a spar-type offshore floating wind turbine. *Journal of Hydrodynamics*, 26(6), 865-874.

[6] Yue, M., Liu, Q., Li, C., Ding, Q., Cheng, S., & Zhu, H. (2020). Effects of heave plate on dynamic response of floating wind turbine Spar platform under the coupling effect of wind and wave. *Ocean Engineering*, 201, 107103.

[7] Robertson, A., Jonkman, J., Masciola, M., Song, H., Goupee, A., Coulling, A., & Luan, C. (2014). Definition of the semisubmersible floating system for phase II of OC4. *National Renewable Energy Laboratory (NREL), Technical Report No. NREL/TP-5000-60601*, Colorado, United States.

[8] Matha, D. (2010). Model development and loads analysis of an offshore wind turbine on a tension leg platform with a comparison to other floating turbine concepts. *National Renewable Energy Laboratory (NREL), Technical Report No. NREL/SR-500-45891*, Colorado, United States.

[9] Goupee, A. J., Koo, B., Lambrakos, K., & Kimball, R. (2012). Model tests for three floating wind turbine concepts. *In Offshore technology conference.* Texas, United States.

[10] Vijfhuizen, W. J. M. (2006). Design of a wind and wave power barge. *Universities of Glasgow and Strathclyde* (*Master thesis),* Glasgow, Scotland.

[11] Bak, C., Bitsche, R., Yde, A., Kim, T., Hansen, M. H., Zahle, F. & Behrens, T. (2012). Light Rotor: The 10-MW reference wind turbine. I*n EWEA 2012-European Wind Energy Conference & Exhibition. European Wind Energy Association (EWEA)*, Copenhagen, Denmark

[12] Velarde, J (2016). Design of monopile foundations to support the DTU 10 MW offshore wind turbine. *Norwegian University of Science and Technology (Master thesis)*, Trondheim, Norway.

[13] Azcona, J., Vittori, F., Schmidt. U., Svanije, F., Kapogiannis, G., Karvelas, X. & Manolas, D. (2017). Design Solutions for 10 MW Floating Offshore Wind Turbines. *INNWIND. EU, Deliverable D*4.

[14] Yu, W., Müller, K., Lemmer, F., Bredmose, H., Borg, M., Sanchez, G., & Landbo, T. (2017). Public Definition of the Two LIFES50+ 10MW Floater Concepts. *LIFES50+ Deliverable, 4*.

[15] Uzunoglu, E., & Soares, C. G. (2020). Hydrodynamic design of a free-float capable tension leg platform for a 10 MW wind turbine. *Ocean Engineering*, 197, 106888.

[16] Armesto, J. A., Jurado, A., Guanche, R., Couñago, B., Urbano, J., & Serna, J. (2018, June). Telwind: Numerical analysis of a floating wind turbine supported by a two bodies platform. *In ASME 2018 37th International Conference on Ocean, Offshore and Arctic Engineering*. Madrid, Spain.

[17] Wen, B., Tian, X., Dong, X., Peng, Z., & Zhang, W. (2017). Influences of surge motion on the power and thrust characteristics of an offshore floating wind turbine. *Energy*, 141, 2054-2068.

[18] Antonutti, R., Peyrard, C., Johanning, L., Incecik, A., & Ingram, D. (2016). The effects of wind-induced inclination on the dynamics of semi-submersible floating wind turbines in the time domain. *Renewable Energy*, 88, 83-94.

[19] Liu, Y., Xiao, Q., Incecik, A., Peyrard, C., & Wan, D. (2017). Establishing a fully coupled CFD analysis tool for floating offshore wind turbines. *Renewable Energy*, 112, 280-301.

[20] Dai, J., Hu, W., Yang, X., & Yang, S. (2018). Modeling and investigation of load and motion characteristics of offshore floating wind turbines. *Ocean Engineering*, 159, 187-200.

[21] Cheng, P., Huang, Y., & Wan, D. (2019). A numerical model for fully coupled aero-hydrodynamic analysis of floating offshore wind turbine. *Ocean Engineering*, 173, 183-196.

[22] Wen, B., Tian, X., Zhang, Q., Dong, X., Peng, Z., Zhang, W., & Wei, K. (2019). Wind shear effect induced by the platform pitch motion of a spar-type floating wind turbine. *Renewable energy*, 135, 1186-1199.

[23] IEC. (2009), IEC 61400-3: Wind Turbines Part 3: Design requirements for offshore wind turbines, *International Electrotechnical Commission*, 2009.

[24] Jonkman, J., Butterfield, S., Musial, W., & Scott, G. (2009). Definition of a 5-MW reference wind turbine for offshore system development. *National Renewable Energy Laboratory (NREL), Technical Report NREL/TP-500-38060*, Colorado, United States.

[25] Bak, C., Zahle, F., Bitsche, R., Kim, T., Yde, A., Henriksen, L. C., & Natarajan, A. (2013). Description of the DTU 10 MW Reference Wind Turbine. *DTU Wind Energy Report-I-0092*. Roskilde Denmark.

[26] Hansen, M. H., & Henriksen, L. C. (2013). Basic DTU wind energy controller. *DTU Wind Energy Report-E-0028*. Roskilde Denmark.

[27] Wendt, F., Robertson, A., Jonkman, J., & Andersen, M. T. (2016). Verification and validation of the new dynamic mooring modules available in FAST v8 *National Renewable Energy Laboratory (NREL), Technical Report No. NREL/CP-5000-65822*, Colorado, United States.

[28] Jonkman, J., Robertson, A. N., & Hayman, G. (2014). HydroDyn User's Guide and Theory Manual. *National Renewable Energy Laboratory (NREL), Technical Report*, Colorado, United States.

[29] Ifremer. Marine Data Portal, French Research Institute for the Exploitation of the Sea, Online: http://data.ifremer.fr/pdmi/portalssearch/main. Data Accessed: May 2020.

[30] Jonkman, B. J., & Buhl Jr, M. L. (2006). TurbSim user's guide. *National Renewable Energy Laboratory (NREL), Technical Report No. NREL/TP-500-39797*, Colorado, United States.

[31] Pierson Jr, W. J., & Moskowitz, L. (1964). A proposed spectral form for fully developed wind seas based on the similarity theory of SA Kitaigorodskii. *Journal of geophysical research*, 69(24), 5181-5190.

[32] Kvittem, M. I., & Moan, T. (2015). Time domain analysis procedures for fatigue assessment of a semi-submersible wind turbine. *Marine Structures*, 40, 38-59.